GDCh Research Article Angewandte International Edition Chemie www.angewandte.org

How to cite: *Angew. Chem. Int. Ed.* **2024**, e202412691
doi.org/10.1002/anie.202412691

Solar Cells

Nonfullerene Acceptors Bearing Spiro-Substituted Bithiophene Units in Organic Solar Cells: Tuning the Frontier Molecular Orbital Distribution to Reduce Exciton Binding Energy

Kai Wang, Seihou Jinnai, Takumi Urakami, Hirofumi Sato, Masahiro Higashi, Sota Tsujimura, Yasuhiro Kobori, Rintaro Adachi, Akira Yamakata, and Yutaka Ie**

Abstract: The development of nonfullerene acceptors (NFAs), represented by **ITIC**, has contributed to improving the power conversion efficiency (PCE) of organic solar cells (OSCs). Although tuning the electronic structures to reduce the exciton binding energy (E_b) is considered to promote photocharge generation, a rational molecular design for NFAs has not been established. In this study, we designed and developed two **ITIC**-based NFAs bearing spiro-substituted bithiophene or biphenyl units (named **SpiroT-DCI** and **SpiroF-DCI**) to tune the frontier molecular orbital (FMO) distribution of NFAs. While the highest occupied molecular orbitals (HOMOs) of **SpiroF-DCI** and **ITIC** are delocalized in the main π-conjugated framework, the HOMO of **SpiroT-DCI** is distributed on the bithiophene unit. Reflecting this difference, **SpiroT-DCI** exhibits a smaller E_b than either **SpiroF-DCI** or **ITIC**, and exhibits greater external quantum efficiency in single-component OSCs. Furthermore, **SpiroT-DCI** shows improved PCEs for bulk-heterojunction OSCs with a donor of PBDB-T, compared with that of either **SpiroT-DCI** or **ITIC**. Time-resolved spectroscopy measurements show that the photo-induced intermolecular charge separation is effective even in pristine **SpiroT-DCI** films. This study highlights the introduction of spiro-substituted bithiophene units that are effective in tuning the FMOs of **ITIC**, which is desirable for reducing the E_b and improving the PCE in OSCs.

Introduction

Organic solar cells (OSCs) continue to show promise as a next-generation energy source due to advantageous attributes such as large-area fabrication, a light weight, flexibility, and the potential for large-scale manufacturing.[1–6] These unique properties suggest utility for practical applications such as in agrivoltaics,[7–10] which has led to much investigation in recent years. The active layer of OSCs consists of a bulk-heterojunction (BHJ) structure composed of two organic semiconductors: a hole-transporting material (donor) and an electron-transporting material (acceptor).[11–13]

[*] K. Wang, S. Jinnai, Y. Ie
The Institute of Scientific and Industrial Research (SANKEN)
Osaka University
8-1 Mihogaoka, Ibaraki, Osaka 567-0047, Japan
E-mail: jinnai@sanken.osaka-u.ac.jp
yutakaie@sanken.osaka-u.ac.jp

S. Jinnai, Y. Ie
Innovative Catalysis Science Division
Institute for Open and Transdisciplinary Research Initiatives (ICS-OTRI)
Osaka University
2-1 Yamadaoka, Suita, Osaka 565-0871, Japan

T. Urakami, H. Sato
Department of Molecular Engineering, Graduate School of Engineering
Kyoto University
Nishikyo-ku, Kyoto 615-8510, Japan

H. Sato
Fukui Institute for Fundamental Chemistry
Kyoto University
Takano Nishihirakicho 34–4, Sakyo-ku, Kyoto 606-8103, Japan

M. Higashi
Department of Complex Systems Science
Graduate School of Informatics
Nagoya University
Furo-cho, Chikusa-ku, Nago-ya 464-8601, Japan

S. Tsujimura
Department of Chemistry
Graduate school of Science
Kobe University
1-1 Rokkodai-cho, Nada-ku, Kobe, Hyogo, 657-8501, Japan

Y. Kobori
Molecular Photoscience Research Center
Kobe University
1-1 Rokkodai-cho, Nada-ku, Kobe, Hyogo, 657-8501, Japan

R. Adachi, A. Yamakata
Graduate School of Natural Science & Technology
Okayama University
3-1-1 Tsushima-naka, Okayama 700-8530, Japan

The combination of high-performance donors with a donor-acceptor configuration and nonfullerene acceptors (NFAs) has increased the power conversion efficiency (PCE) of single-junction OSCs to a remarkable benchmark of more than 19 %.[14,15] Focusing on NFAs has led to the utilization of fused structures in the central portion and electron-withdrawing functional groups at both terminal positions of conjugated frameworks, which has been established as an effective molecular design.[16–19] However, a molecular design based on the electronic structures should also be considered to further improve solar cell performance in terms of charge-carrier generation.

Organic semiconductors generally possess a relatively small dielectric constant (ε_r) and thus the hole-electron pairs formed by photoexcitation are tightly bound in a molecule via the force of Coulomb attraction.[20–23] The energy required to dissociate excitons into free-charge carriers is called the exciton binding energy (E_b). E_b is classically expressed with basic parameters by equation (1)[24]:

$$E_b \approx \frac{e^2}{4\pi\varepsilon_0\varepsilon_r R} \quad (1)$$

In equation (1), e is the elementary charge, ε_0 is the vacuum dielectric constant, and R is the average electron-hole distance in the molecule. If the E_b of semiconductors can be reduced, excitons generated in BHJ OSCs will be more effectively dissociated due to a smaller donor/acceptor energy offset.[25–27] Therefore, reducing the E_b of organic semiconductors by increasing the ε_r and extending the conjugation or introduction of polarizable units is regarded as a rational approach (Figure 1, left). [28–32] Zhang *et al.* reported that enhancement of the hole/electron delocalization via polymerization of a small π-conjugated compound led to a reduction in the E_b.[31] Li *et al.* showed that asymmetric glycolate substitution onto Y6-based compounds, named Y6-4O, successfully reduced its E_b. Y6-4O showed an improved external quantum efficiency (EQE) of 1.4 % in single-component (SC) OSCs (Figure S1 in the Supporting Information).[32] On the other hand, according to equation (1), the E_b of organic semiconductors is also expected to decrease by increasing the R in the photoexcited state. Photoinduced charge separation in organic semiconductors is generally mediated by the S_1 excited state, in which one electron is transitioned from the the highest occupied molecular orbital (HOMO) to the lowest unoccupied molecular orbital (LUMO) in a molecule. Therefore, we considered that the increased R can be attained by detaching the spatial distribution of the HOMO and LUMO of semiconductor molecules. However, the development of organic semiconductors with a tuned R in the S_1 state has not been reported.

Recently, we reported that the introduction of spiro-substituted biphenyl units has advantages that improve the OSC characteristics of a non-fused type NFA **TT-FT-DCI** (Figure 1).[33] The π-extended biphenyl unit adjusts the frontier molecular orbital energy level by modifying the chemical structure. Replacing the biphenyl unit with an electron-donating bithiophene unit tunes the shallow HOMO energy level, which leads to a shift in the electronic distribution of the HOMO from the conjugated backbone to the bithiophene unit (See below for details). Therefore, we hypothesized that the tuning of R could be achieved by utilizing the structural feature of a perpendicular orientation in a spiro-substituted unit against a π-conjugated main framework. To investigate the effectiveness of this molecular design, we selected a representative fused-ring type of **ITIC** framework in this study.[16,17,34] Therefore, we designed new **ITIC**-based NFAs **SpiroT-DCI** and **SpiroF-DCI**, in which bithiophene and biphenyl skeletons are spiro-substituted into the **ITIC** (Figure 1, right). In this study, we investigated the effect of electronic structures on R, E_b, and OSC characteristics.

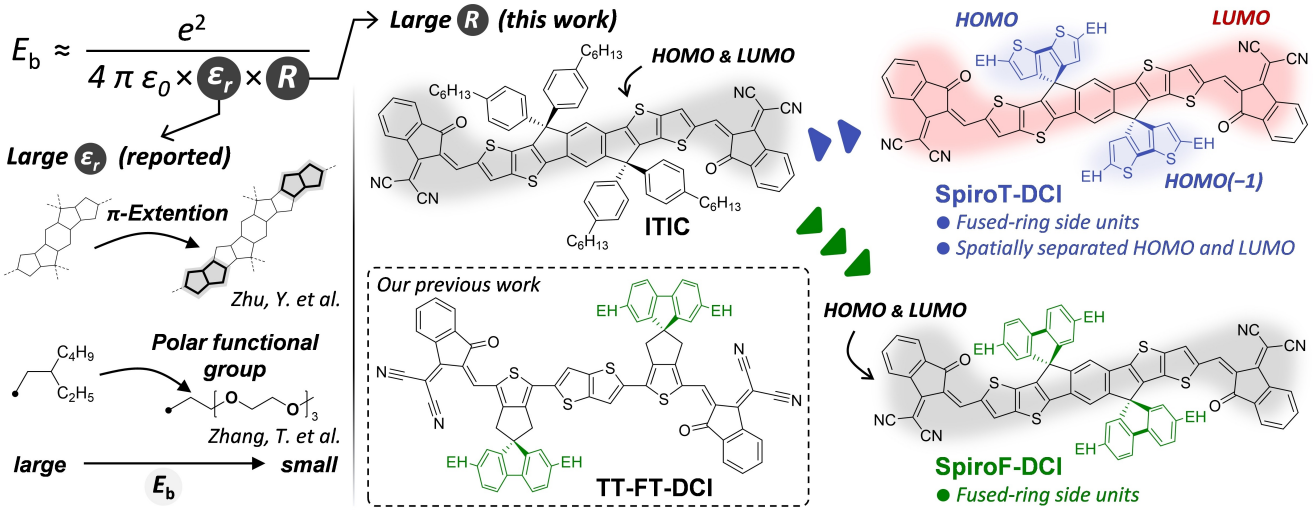

Figure 1. Molecular design to reduce the E_b of organic semiconductors and chemical structures of **SpiroT-DCI**, **SpiroF-DCI**, and **ITIC**.

Results and Discussion

Synthesis of Compounds

The synthetic routes to **SpiroT-DCI** and **SpiroF-DCI** are shown in Scheme 1. The starting material **1** was prepared using a previously reported procedure.[35] Compound **2a** was obtained in a 65 % yield via the nucleophilic addition of a lithiated bithiophene derivative of **1**. Treatment of compounds **2a** with boron tribromide (BBr_3) gave **SpiroT** in an 86 % yield. The formylation of **2a** afforded **SpiroT-CHO**, which was subjected to Knoevenagel condensation with 1-(dicyanomethylene)-3-indanone to give **SpiroT-DCI**. Compound **SpiroF-DCI** was synthesized in the same manner. Due to the presence of 2-ethylhexyl groups, both compounds showed sufficient solubility in typical process solvents such as 1,2-dichlorobenzene (*o*-DCB), chlorobenzene, and chloroform. The synthesis details, structural characterization, ^1H and ^{13}C NMR spectra, and high-resolution mass spectrometry data are supplied in the SI.

The thermal properties of **SpiroT-DCI** and **SpiroF-DCI** were evaluated using thermogravimetric analysis (TGA) under a nitrogen atmosphere. As shown in Figure S2, the thermal decomposition temperatures (T_d) at a 5 % weight loss of **SpiroT-DCI** and **SpiroF-DCI** are 319 and 338 °C, respectively. These T_d values indicate that these compounds possess sufficient thermal stabilities for application to OSCs.

Theoretical Investigation

To gain insight into the effect that spiro-substituted units exert on electronic structures, theoretical calculations using density functional theory (DFT) and time-dependent DFT (TD-DFT) methods were performed. Ground-state and excited-state geometries were optimized by B3LYP and ω-tuned ωB97XD functions, respectively, using a 6–31G(d,p) basis set.[36,37] As shown in Figure S3, the conjugated backbones of **SpiroT-DCI** and **SpiroF-DCI** showed a planar configuration similar to that of **ITIC**. The bithiophene and biphenyl units in **SpiroT-DCI** and **SpiroF-DCI** are perpendicularly oriented to the indacenodithenothiophene (IDTT, highlighted in Scheme 1) backbone due to the sp^3 hybridized spiro carbon atom.

As shown in Figure 2a, **SpiroF-DCI** and **ITIC** showed overlapped HOMO/LUMO distributions on the IDTT backbone. By contrast, **SpiroT-DCI** exhibited detached HOMO/LUMO distributions with the HOMO localized mainly on the bithiophene and the LUMO localized on the IDTT and dicyanomethylideneindanone (DCI) terminal units. The different HOMO distributions between **SpiroT-DCI** and **SpiroF-DCI** stem from the difference in the HOMO energy levels of bithiophene and biphenyl: The HOMO energy level of bithiophene is shallower than that of the **ITIC** backbone, whereas biphenyl possesses a deeper HOMO energy than that of the **ITIC** backbone. As a result, the electron orbital distribution corresponding to the HOMO of **SpiroF-DCI** appeared at the HOMO–2 of **SpiroT-DCI**. Reflecting this HOMO distribution, the HOMO energy level (E_{HOMO}) of **SpiroT-DCI** was calculated to be −5.26 eV, which is obviously upshifted compared with those of **SpiroF-DCI** (−5.44 eV) and **ITIC** (−5.46 eV). On the other hand, the LUMO energy levels (E_{LUMO}) for these compounds are almost identical values of around −3.35 eV.

To further understand the difference in electronic structure caused by structural variations, we analyzed the hole and electron distributions for the S_1 state (Table S1). Figure 2b shows the isosurfaces of the hole and electron distributions in the S_1 state.[38,39] Notably, the hole and electron of **SpiroT-DCI** were separately populated on the bithiophene units and on the IDTT backbone, respectively. By contrast, both the hole and the electron of **SpiroF-DCI**

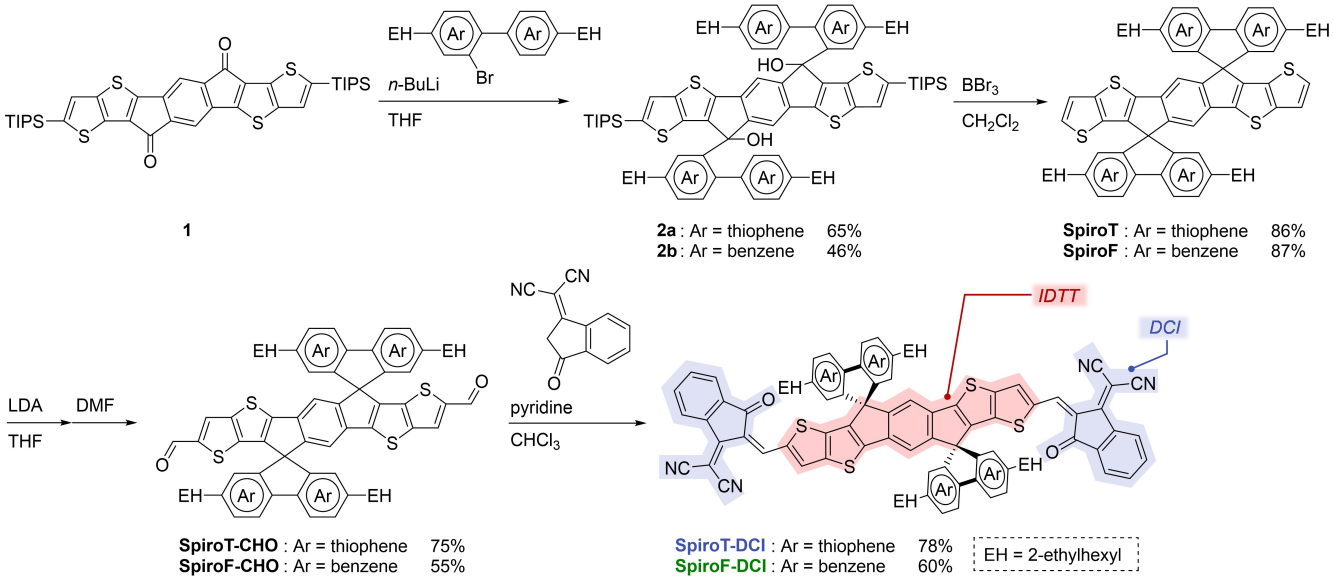

Scheme 1. Synthetic routes to **SpiroT-DCI** and **SpiroF-DCI**.

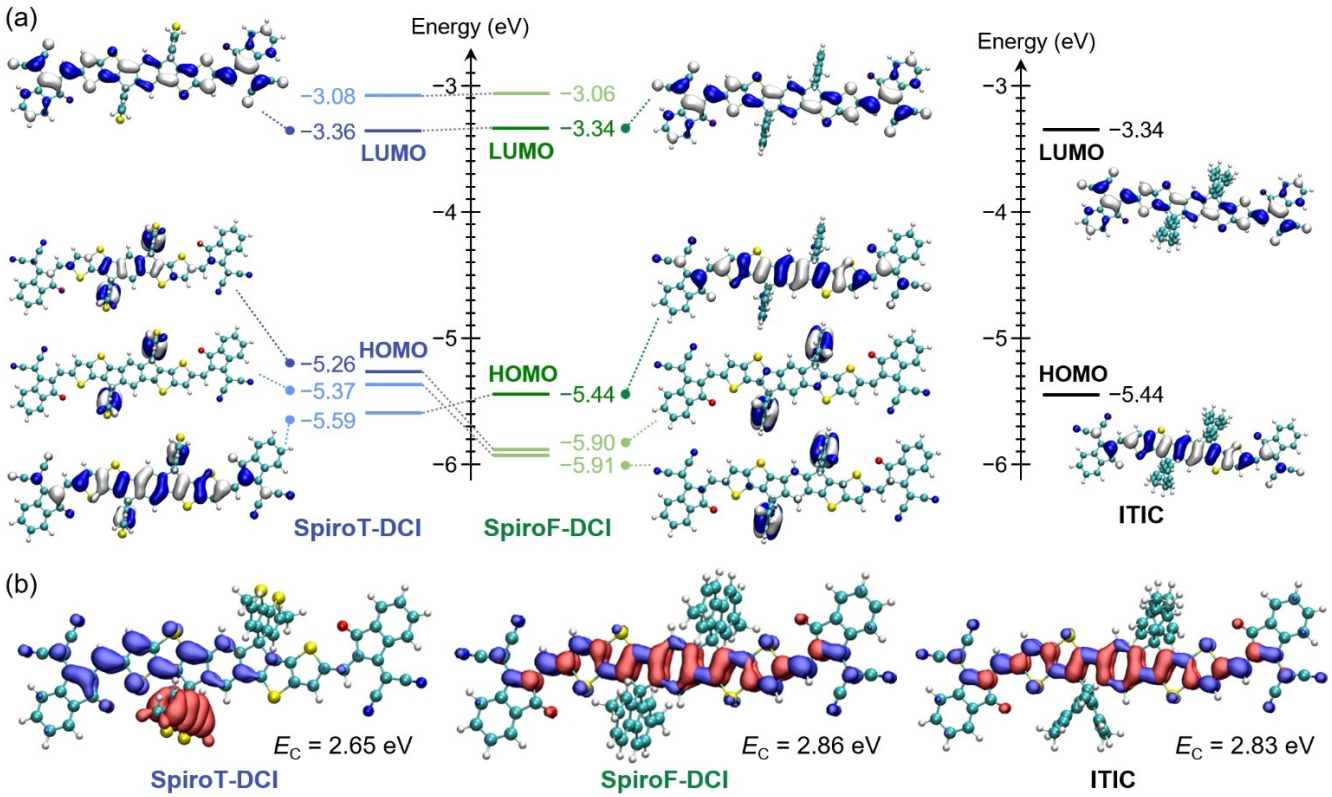

Figure 2. (a) Distribution and energy level of molecular orbitals. (b) Distributions of the hole (red) and electron (blue) for S_1 state.

and **ITIC** dominantly populated the IDTT backbone. The distance between hole and electron centroids was calculated to be 3.612 Å for **SpiroT-DCI**, 0.002 Å for **SpiroF-DCI**, and 0.052 Å for **ITIC**, indicating that **SpiroT-DCI** forms S_1 state with larger R compared to the other compounds. These results indicate that the exciton in the S_1 of **SpiroT-DCI** is more favorable to the formation of a CT state rather than a local excited (LE) state. Furthermore, the Coulomb attraction energies (E_C) based on these distributions for **SpiroT-DCI**, **SpiroF-DCI**, and **ITIC** were calculated to be 2.65, 2.86 and 2.83 eV, respectively.[40] The apparently smaller E_C for **SpiroT-DCI** suggests that charge separation in the excited state might be more facile compared with that of either **SpiroF-DCI** or **ITIC**, which is likely beneficial for the photon-to-current conversion process in OSCs.

Electrochemical and Photophysical Properties

The electrochemical properties of **SpiroT-DCI** and **SpiroF-DCI**, as well as reference compound **ITIC**, were investigated using differential pulse voltammetry (DPV). As shown in Figure S4a, these molecules exhibited a similar reduction pattern, where the first reduction peaks of **SpiroT-DCI**, **SpiroF-DCI**, and **ITIC** were 0.95, 0.95, and 0.92 V, respectively, vs. the ferrocene/ferrocenium (Fc/Fc^+) couple.[41] As shown by the oxidation peaks in Figure S4b, **SpiroT-DCI** (0.56 V) possesses a lower oxidation potential than that of either **SpiroF-DCI** (0.74 V) or **ITIC** (0.76 V). The E_{HOMO} and E_{LUMO} values of **SpiroT-DCI**, **SpiroF-DCI**, and **ITIC** were calculated from the oxidation and reduction peaks to be −5.37/−3.83, −5.54/−3.83, and −5.54/−3.85 eV, respectively (Table 1). These values are qualitatively consistent with the DFT results shown in Figure 2, and experimentally demonstrate the upshifted HOMO energy level of **SpiroT-DCI**.

Table 1: Physical properties of **SpiroT-DCI**, **SpiroF-DCI**, and **ITIC**.

Compounds	λ_{max}^{sol} (nm)[a]	λ_{max}^{film} (nm)	λ_{onset}^{film} (nm)	E_g^{opt} (eV)[b]	E_{HOMO} (eV)[c]	E_{LUMO} (eV)[c]	IP (eV)[d]	EA (eV)[e]	E_b (eV)[f]
SpiroT-DCI	693	709	785	1.58	−5.37	−3.83	5.75	3.85	0.32
SpiroF-DCI	680	695	764	1.62	−5.54	−3.83	5.88	3.86	0.40
ITIC	679	697	765	1.62	−5.54	−3.85	5.88	3.85	0.41

[a] In chloroform. [b] E_g^{opt} was calculated by 1240 / λ_{onset}^{film}. [c] Determined by DPV in *o*-DCB/acetonitrile containing 0.1 M of tetrabutylammonium hexafluorophosphate ($TBAPF_6$). [d] Estimated using PYS. [e] Estimated using LEIPS. [f] $E_b = EA - IP - E_g^{opt}$.

Low-energy inverse photoemission spectroscopy (LEIPS)[42–44] and photoelectron yield spectroscopy (PYS)[45] were conducted to determine the electron affinity (EA) and ionization potential (IP) of **SpiroT-DCI**, **SpiroF-DCI**, and **ITIC** in films. As shown in Figures 3a and 3b, the EA values of these molecules were similar – approximately 3.85 eV. The IP values for **SpiroT-DCI**, **SpiroT-DCI**, and **ITIC** were found to be 5.75, 5.88 and 5.88 eV, respectively (Table 1). This result indicates that the presence of the bithiophene units could effectively raise the HOMO energy level while leaving the LUMO energy level unaffected, which is consistent with the electrochemical results and DFT calculations. Based on the EA value of 3.18 eV for PBDB-T determined by the same method (Figure S5), the EA offsets between these NFAs and PBDB-T were calculated to be around 0.7 eV, which meets the energy level offset requirement for efficient charge separation at donor-acceptor interfaces.[46,47]

The UV/Vis absorption spectra of **SpiroT-DCI**, **SpiroF-DCI**, and **ITIC** in chloroform solutions and films appear in Figures S6 and 3c. In the solution spectra, **SpiroF-DCI** and **ITIC** showed absorption bands at almost an identical wavelength with maximum absorption peaks (λ_{max}^{sol}) at 680 and 679 nm, respectively. By contrast, **SpiroT-DCI** exhibited a red-shifted absorption band with a λ_{max}^{sol} at 693 nm. The molar extinction coefficient (ε) of **SpiroT-DCI**, **SpiroF-DCI**, and **ITIC** were found to be 1.40×10^5, 1.95×10^5, and 2.12×10^5 L mol^{-1} cm^{-1}, respectively (Figure S6a). The relatively smaller ε value for **SpiroT-DCI** was consistent with the TD-DFT results (Table S1). All the compounds in films exhibited a red-shift of more than 15 nm, indicating the appearance of intermolecular interactions in the solid state. The optical energy gap (E_g^{opt}) based on the onset of the absorption spectra in films was estimated to be 1.58 eV for **SpiroT-DCI**, 1.62 eV for **SpiroF-DCI**, and 1.62 eV for **ITIC** (Table 1). As shown in Figure S7, the photoluminescence (PL) spectra of **SpiroT-DCI** exhibited lower PL intensities compared with those of either **SpiroF-DCI** or **ITIC** in both solutions and films. The Stoke's shifts of **SpiroT-DCI**, **SpiroF-DCI**, and **ITIC** in solution were calculated to be 930, 820, and 820 cm^{-1}, respectively. The observed phenomena of **SpiroT-DCI** are explained as typical characteristics of CT excited states.[48–50]

Based on the EA, IP, and E_g^{opt} values, we used equation (2) to estimate the E_b values for **SpiroT-DCI**, **SpiroF-DCI**, and **ITIC** in films[28,29,51].

$$E_b = EA - IP - E_g^{opt} \quad (2)$$

As shown in Figure 3d, **SpiroT-DCI** possesses a smaller E_b value of 0.32 eV compared with that of either **SpiroF-DCI** (0.40 eV) or **ITIC** (0.41 eV). This qualitatitve trend was consistent with the calculated E_C values (Figure 2b). This result indicates that excitons derived from **SpiroT-DCI** tend to form a charge-separated state, making the CT state more favorable. This is beneficial for accelerating the photon-to-current conversion.

OSC Characteristics

To examine the influence of the E_b values on device performance, we first investigated the photon-to-current conversion function using SC-OSC devices by utilizing **SpiroT-DCI**, **SpiroF-DCI**, or **ITIC** as the active layer (Figure 4a). Details of the fabrication and evaluation procedure of SC-OSC are provided in the SI. The current density (J)–voltage (V) characteristics of SC-OSCs under an air mass of 1.5G using a solar simulator lamp (100 mW cm^{-2}) are shown in Figure 4b. The SC-OSCs based on **SpiroT-DCI** showed a PCE of 0.06 % with a short-circuit current density (J_{sc}) of 0.51 mA cm^{-2}. By contrast, a **SpiroF-DCI**- and **ITIC**-based device showed significantly lower PCE and J_{sc} values (Table S2). As shown in Figure 4c, the maximum external quantum efficiency (EQE_{max}) of **SpiroT-DCI** was found to be 3.6 %, which is higher than those of **SpiroF-DCI** (0.7 %), **ITIC** (0.6 %), or Y6-4O (1.4 %).[32] This result indicates that **SpiroT-DCI** has a higher level of photocarrier generation characteristics, compared with those of either **SpiroF-DCI** or **ITIC**.

The photovoltaic characteristics of BHJ-OSCs with **SpiroT-DCI** and **SpiroF-DCI** as acceptors were investigated using an inverted configuration of ITO/ZnO/PBDB-T[52] (CAS Registry No. 1415929-80-4):acceptor/MoO_3/Ag (Figure 4d),[53] where the donor polymer of PBDB-T was selected due to its complemental absorption with these

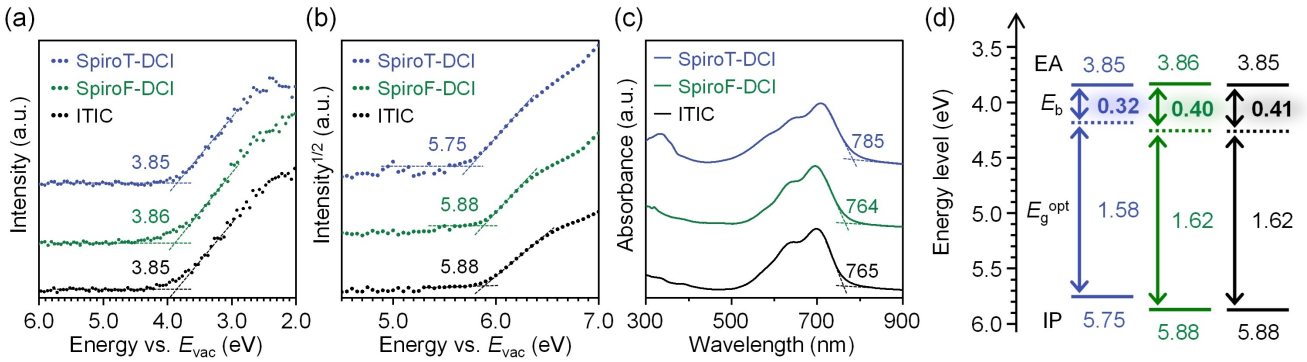

Figure 3. (a) LEIPS, (b) PYS, (c) UV/Vis absorption spectra, and (d) Energy level diagrams of **SpiroT-DCI**, **SpiroF-DCI**, and **ITIC** in pristine films.

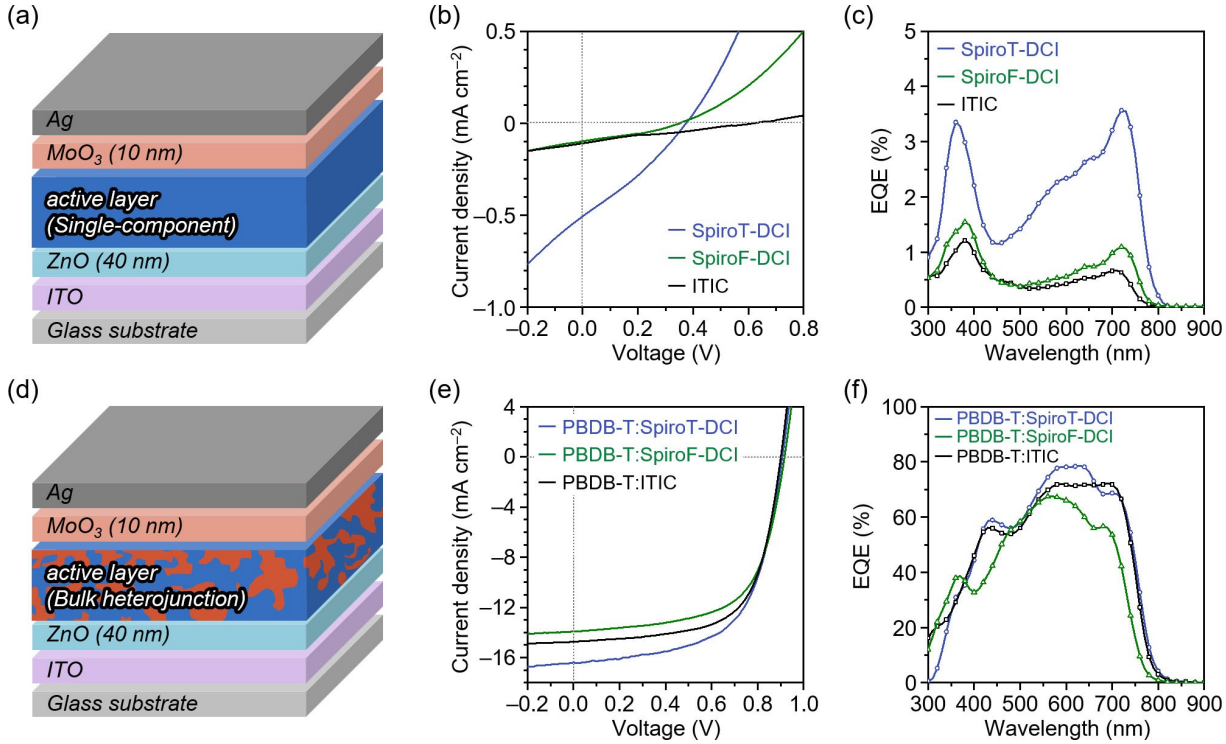

Figure 4. (a) Device structure, (b) *J*–*V* curves, and (c) EQE spectra for SC-OSC devices. (d) Device structure, (e) *J*–*V* curves, and (f) EQE spectra for BHJ-OSC devices.

acceptors. The details of the fabrication conditions and device characteristics are provided in Tables S3–S7 in the SI. Figure 4e shows the *J*–*V* characteristics of the best-performing BHJ-OSCs, and the key OSC parameters are summarized in Table 2. The best PCEs of the PBDB-T:**SpiroT-DCI**, PBDB-T:**SpiroF-DCI**, and PBDB-T:**ITIC** films were 9.08, 8.04, and 8.62 %, respectively. As expected, the PBDB-T:**SpiroT-DCI**-based device showed a higher PCE value compared with those of either PBDB-T:**SpiroF-DCI** or PBDB-T:**ITIC**, which was due mainly to the increased J_{sc}. The EQE spectra of the PBDB-T:**SpiroT-DCI**-based device showed EQE responses between 400 and 800 nm, which were higher than those of PBDB-T:**SpiroF-DCI** and PBDB-T:**ITIC**. The PBDB-T:**SpiroT-DCI**-based device attained an EQE_{max} of 79 % at 630 nm (Figure 4f). The integrated current densities from the EQE curves match well with the integrated current density values from the *J*–*V* tests (within a 5 % error range), which indicates the good accuracy and reliability of the proposed performance parameters. These results indicate that **SpiroT-DCI** has potential for use as an organic semiconductor for OSCs.

To estimate the hole and electron mobilities of the blend films, the space-charge limited current (SCLC) was investigated.[54–56] The *J*–*V* characteristics for the PBDB-T:**SpiroT-DCI**, PBDB-T:**SpiroF-DCI**, and PBDB-T:**ITIC** films are shown in Figure S8. Based on Child's law, the hole and electron mobilities (μ_h and μ_e) were calculated and are listed in Table S8. The relatively small differences between μ_h and μ_e among blend films indicate that the carrier transport characteristics make only limited contributions to the photocurrent.

To investigate the exciton dissociation and charge generation efficiencies of BHJ-OSCs, we plotted the photocurrent density (J_{ph}) against the effective applied voltage (V_{eff}).[57,58] As shown in Figure S9, the J_{ph} for the PBDB-T:**SpiroT-DCI**-based device was higher than that of either the PBDB-T:**SpiroF-DCI** or PBDB-T:**ITIC** devices, indicating that the overall photo-charge generation efficiency for PBDB-T:**SpiroT-DCI** was higher than that of the other blend films. The J_{ph} showed saturation when V_{eff} exceeded ~1 V for all devices. Based on the equation $P_{coll}=J_{sc}/J_{sat}$, the charge carrier collection probabilities (P_{coll}) were estimated

Table 2: BHJ-OSC characteristics of **SpiroT-DCI**, **SpiroF-DCI**, and **ITIC**.

Active layer	PCE (%)	J_{sc} (mA cm^{-2})	V_{oc} (V)	FF (%)	EQE_{max} (%)
PBDB-T:**SpiroT-DCI**	9.08 (8.93 ± 0.13)	16.39 (16.47 ± 0.29)	0.91 (0.90 ± 0.01)	61 (60 ± 1)	78.6
PBDB-T:**SpiroF-DCI**	8.04 (7.78 ± 0.16)	13.93 (13.34 ± 0.39)	0.92 (0.92 ± 0.00)	63 (63 ± 1)	68.4
PBDB-T:**ITIC**	8.62 (8.41 ± 0.13)	14.73 (14.33 ± 0.28)	0.90 (0.90 ± 0.01)	65 (65 ± 1)	72.2

The values in parentheses indicate the mean and standard deviation of five independent devices in Tables S5–S7.

to be 84% for PBDB-T:**SpiroT-DCI**, 84% for PBDB-T:**SpiroF-DCI**, and 86% for PBDB-T:**ITIC**. The almost identical P_{coll} values indicate limited differences in the charge-transport and collection processes under short-circuit conditions.

The surface morphologies of the optimized PBDB-T:**SpiroT-DCI**, PBDB-T:**SpiroF-DCI**, and PBDB-T:**ITIC** films were investigated via atomic force microscopy (AFM). Figure S10 shows that all the blend films exhibited a uniform and relatively smooth surface morphology, and lists arithmetical mean deviation (R_a) surface roughness values of 2.2, 1.7, and 2.0 nm for PBDB-T:**SpiroT-DCI**, PBDB-T:**SpiroT-DCI**, and PBDB-T:**ITIC**, respectively. The crystallinities were investigated using X-ray diffraction (XRD) measurements. As shown in Figure S11, all the blend films exhibited weak diffraction peaks between $2\theta = 4–5°$ (corresponds to a lattice spacing of 1.8–2.2 nm) in both out-of-plane and in-plane directions. The diffraction peaks approximate to the longitudinal length of the acceptor molecules, which indicates that all the blend films have an isotropic lamellar arrangement for acceptors.

To gain further insight into the arrangement of acceptors, molecular dynamics (MD) simulations were performed for **SpiroT-DCI**, **SpiroF-DCI**, and **ITIC**. The computational details of the MD simulations are provided in the SI. Figure 5a shows the radial distribution functions (RDFs) between acceptor sites. The RDFs of **SpiroT-DCI**, **SpiroF-DCI**, and **ITIC** are similar. The large peaks at ~4 Å indicate the stacking between acceptor-acceptor (A-A) sites, which is consistent with previous studies of **ITIC** films.[59,60] Next, the distributions of the distances between electron-donating IDTT sites in the A-A stacking structures were analyzed (Figure 5b). The largest peaks at ~20 Å correspond to J-type molecular stacking, and indicate that J-type molecular stacking is dominant in **SpiroT-DCI**, **SpiroF-DCI**, and **ITIC** films. The short distance between donor sites corresponds to a V-type stacking structure. The distribution for **ITIC** is broader than those for either **SpiroT-DCI** or **SpiroF-DCI** due to the flexible side chains of **ITIC**. The rigid side chains of **SpiroT-DCI** and **SpiroF-DCI** preferably adopt a specific V-type stacking structure. The similar distribution between **SpiroT-DCI** and **SpiroF-DCI** indicates that the higher PCE of **SpiroT-DCI** could originate from the difference in electronic structures.

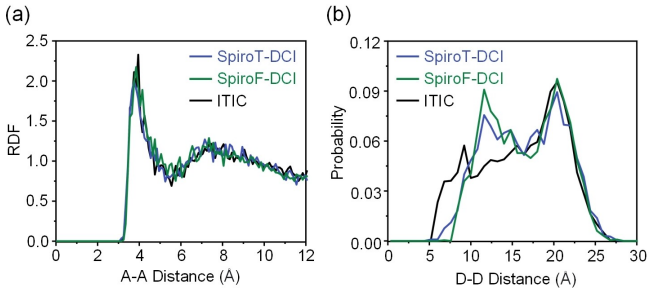

Figure 5. Results of MD simulations. (a) The radial distribution functions between acceptor-acceptor sites. (b) The distribution of electron-donating IDTT-IDTT distance in the acceptor-acceptor stacking structures.

Time-resolved Analyses of Exciton Dynamics for Pristine Films

To elucidate the photoinduced responses of **SpiroT-DCI** and **SpiroF-DCI** relative to **ITIC**, transient IR absorption (TR-IR) measurements were conducted (Figures 6 and 7).[61,62] This method is particularly effective for studying intra- and inter-molecular charge transfer processes and for elucidating the behavior of free carriers that contribute to electrical conductivity. This effectiveness arises because intra- and inter-molecular charge transfer processes alter the local electron density within NFA molecules, which changes molecular vibrational frequencies such as those of cyano groups. Additionally, free carriers provide a broad, structureless absorption in the infrared region. Therefore, TR-IR is a crucial tool for investigating intra- and inter-molecular charge transfer and the behavior of free carriers.

As shown in Figure 6a, the photoexcitation of a neat **ITIC** film leads to a negative peak at 2,225 cm^{-1} and two positive peaks at 2,205 and 2,175 cm^{-1}. Previously, we reported that the negative peak is associated with the ground state bleaching of parent CN groups, and the two positive peaks correspond to the S_1 state of **ITIC** and the anionic **ITIC** molecules resulting from intra- and inter-molecular charge separations, respectively.[33] The emergence of these red-shifts in CN indicates an increase in electron density around CN due to photoexcitation, and confirms that intermolecular charge separation occurs even in the absence of a donor layer.

Similar red-shifts were observed for **SpiroT-DCI** (Figure 6b), and although the relative peak intensities at 2,205 and 2,175 cm^{-1} differed significantly, the intensity of 2,175 cm^{-1} is markedly greater than that of 2,205 cm^{-1}, which suggests that intermolecular charge separation is more efficient in **SpiroT-DCI** compared with that in **ITIC**. Analogous results for **SpiroF-DCI** indicate that intermolecular charge separation also occurs (Figure 6c). However, the relative peak intensity at 2,175 cm^{-1} is considerably smaller than at 2,205 cm^{-1}, which indicates a less-frequent intermolecular charge separation in **SpiroF-DCI**, compared with that in either **SpiroT-DCI** or **ITIC**. By considering the peak intensity ratios of 2,175 to 2,205 cm^{-1}, the order for the efficiency of intermolecular charge transfer would be **SpiroT-DCI** > **ITIC** > **SpiroF-DCI**.

To examine how the E_b contributes to photoinduced charge-transfer and charge-separation kinetic behavior in pristine films, we observed time-resolved photoluminescence (PL) decay at room temperature. Figure 8 shows the time-resolved PL spectra (a, c) and time profiles (b, d) for the **SpiroT-DCI** and **SpiroF-DCI** neat films, respectively. Although the PL spectrum shapes are similar between these NFAs, which is characteristic of broad CT band emissions, the PL intensity of the **SpiroT-DCI** film is much weaker than that of the **SpiroF-DCI**

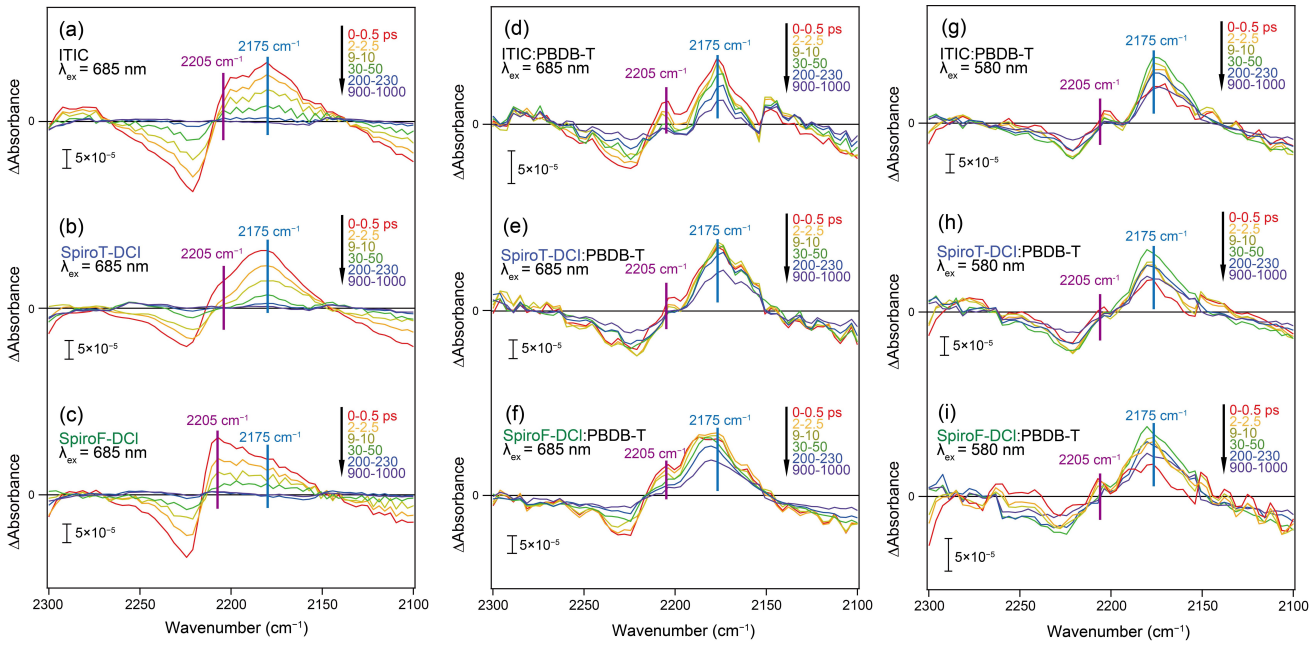

Figure 6. Differential vibrational spectra of CN groups in NFAs after pump pulse irradiation. Neat **ITIC** (a), **SpiroT-DCI** (b), and **SpiroF-DCI** (c) are photoexcited by a 685 nm pump pulse. Additionally, the NFA domain in the blend film with PBDB-T is photoexcited by the same 685 nm pump pulse (panels d–f). PBDB-T within the blend film is selectively photoexcited by a 580 nm pump pulse (panels g–i). Broad absorption by photocarriers was subtracted to extract the change of CN vibrations.[66]

film, which indicates that the more efficient charge-separation may significantly reduce emissions following photoirradiation. Accordingly, the quicker PL decay in **SpiroT-DCI** (Figure 8b) than in **SpiroF-DCI** (Figure 8d) suggests efficient charge generation from the S_1 exciton.[63–65] Based on the above transient absorption results (Figure S12) where free carriers are created in the pristine films, we performed analysis of the time-traces of the PL data as shown by the red lines in Figures 8b and 8d by solving coupled-rate equations, as detailed in the SI (Scheme 2, and Equation S1).

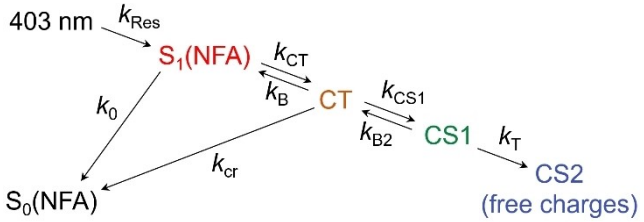

Scheme 2. Kinetic model for analyzing the transient PL profiles after the 403 nm light.

As listed in Table 3, the quicker decay in **SpiroT-DCI** (Figure 8b) is explained by $k_{CS1}=2.8\ ns^{-1}$, while the minor second decay component is rationalized by the thermally activated delayed fluorescence with $k_{B2}=0.7\ ns^{-1}$, which results in a free energy change of $\Delta G_{CS}=-0.07$ eV by using $\Delta G=-k_B T \ln(k_{CS1}/k_{B2})$. On the other hand, the single exponential decay in Figure 8c denotes that the CS rate constant is much smaller in **SpiroF-DCI** – estimated to be $k_{CS1}=0.3\ ns^{-1}$ (Table 3). This is explained by the large E_b (0.40 eV) in **SpiroT-DCI** and is consistent with a small EQE in the SC-OSCs (Figure 4c). Overall, the exergonic CS behavior in the **SpiroT-DCI** neat film is consistent with the small E_b of 0.32 eV for the charge-generation in the neat film.

Time-resolved Analyses of Exciton Dynamics for Blend Films

TR-IR measurements were extended to the blend films with PBDB-T. In these experiments, only the acceptor molecules (**ITIC**, **SpiroT-DCI**, or **SpiroF-DCI**) were excited using 685 nm laser pulses. As shown in Figure 6d, two positive peaks appeared at 2,205 and 2,175 cm^{-1}, which is similar to the observations in pristine **ITIC**

Table 3: Excited state kinetic parameters estimated for neat films of **SpiroT-DCI** and **SpiroF-DCI**.

Film	k_{CT} (ps^{-1})	k_B (ps^{-1})	k_{CS1} (ns^{-1})	k_{B2} (ns^{-1})	k_T (ns^{-1})
SpiroT-DCI	1.0	0.24	2.8	0.7	0.9
SpiroF-DCI	1.1	1.1	0.3	–	–

$k_{Res}=10\ ns^{-1}$, $k_0=2.8\ ns^{-1}$ and $k_{CR}=1.0\ ns^{-1}$ are applied. See the SI.

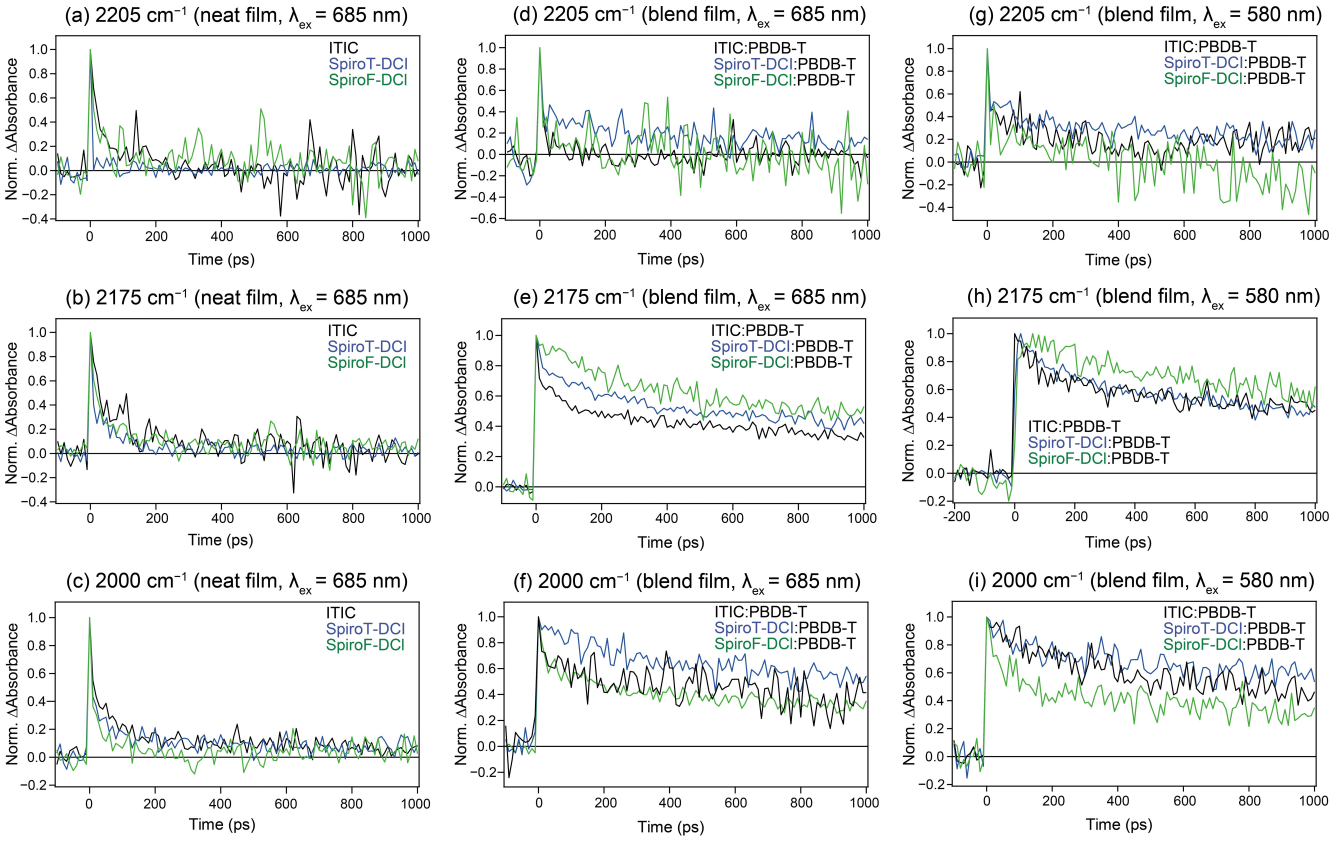

Figure 7. Time profiles for the locally excited (LE) state of NFAs, anionic NFAs, and free electrons in neat and blend films are presented. These profiles were obtained by photoexciting the neat NFA film with a 685 nm pump pulse and measuring at 2,205, 2,175, and 2,000 cm^{-1}, respectively (panels a–c). The NFA domain (panels d–f) and the PBDB-T domain (panels g ~ i) on the blend film with PBDB-T were also selectively photoexcited by a 685 nm and 580 nm pump pulses, respectively. The peak heights at 2,205 and 2,175 cm^{-1} were calculated after subtracting the broad absorptions by free electrons to extract the change of CN vibrations (Figure 6) and those of free electrons were estimated from Figure S12.

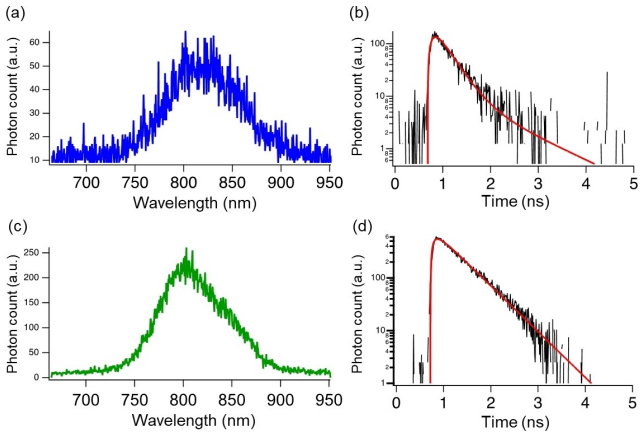

Figure 8. Time-resolved photoluminescence data of neat films of a,b) **SpiroT-DCI** and c,d) **SpiroF-DCI** obtained at room temperature. The spectra in the left panels were obtained by accumulating photon counts at 1 ns with a width of 200 ps.

films. However, the decay of the peak at 2,205 cm^{-1} is accelerated, and the lifetime of the peak at 2,175 cm^{-1} is extended. These findings indicate that intermolecular charge separation is more efficiently facilitated at the donor/acceptor interface.

Consistent observations were made for **SpiroT-DCI** and **SpiroF-DCI**, as shown in Figures 6e and 6f. The lifetime of the peak at 2,175 cm^{-1} in these films also increased, further confirming the enhanced charge separation efficiency due to the formation of the donor/acceptor interface. This result suggests a more effective interaction and charge-transfer dynamics at the interfaces in blend films, compared with that in the pristine films of the acceptors.

The interfacial charge separation was further analyzed by photoexciting the PBDB-T donor layers with a 580 nm pump pulse and monitoring the C–N stretching mode in the NFA layers. In the PBDB-T:**ITIC** blend film, as illustrated in Figure 6g, a negative peak and a positive peak were observed at 2,225 cm^{-1} and 2,175 cm^{-1}, respectively, with a small shoulder at 2,205 cm^{-1}. The small peaks at 2,205 cm^{-1} are attributed to the partial photoexcitation of the **ITIC** layer by the 580 nm pump pulse. More critically, the presence of the 2,175 cm^{-1} peak confirms that electron injection occurs from the PBDB-T layer to the **ITIC** layer, which results in the formation of anionic **ITIC** molecules. Similar

electron injections from the donor to acceptor layers were observed for **SpiroT-DCI** and **SpiroF-DCI**, which indicates that charge separation occurs at the donor/acceptor interface.

To better understand the decay kinetics of photoexcited charge carriers at the donor/acceptor interface, changes in intensity at 2,205, 2,175, and 2,300 cm^{-1} are presented in Figure 7. As shown in Figure 7a, the S_1 state of neat **ITIC**, which is induced by intramolecular charge transfer, exhibits an absorption peak at 2,205 cm^{-1} that diminishes within approximately 100 ps. The anionic **ITIC** state, which is characterized by an absorption peak at 2,175 cm^{-1}, also was diminished within ~100 ps (Figure 7b). However, via the formation of a heterojunction, its lifetime was extended – exceeding 1,000 ps (Figure 7e). This duration is notably longer than that observed in a neat **ITIC** film. These findings indicate that the formation of a donor/acceptor heterojunction extends the lifetime of the anionic **ITIC** state, by comparison with the S_1 state. A similar extension in lifetime for the anionic state is observed in **SpiroT-DCI** and **SpiroF-DCI**, with the lifetimes increasing on the order of **SpiroF-DCI** > **SpiroT-DCI** > **ITIC**. Comparable trends are noted for donor photoexcitation, where the lifetime sequence is **SpiroF-DCI** > **SpiroT-DCI** ≈ **ITIC**. However, the lifetime of these anionic states does not consistently correlate with the PCEs since anions do not participate directly in the charge-carrier transport that is necessary for current flow; instead, electrons remain bound within the molecules and thus are immobile. Conversely, free carriers, which are essential for generating photocurrent, can be analyzed by observing their broad, structureless absorption in the mid-IR region, particularly at 2,000 cm^{-1}, which is an absorption peak that is off-resonant to the C–N vibration. As depicted in Figure 7c, the lifetimes of free electrons generated by the photoexcitation of neat NFAs follow the order of **SpiroT-DCI** > **ITIC** > **SpiroF-DCI**. A similar sequence is observed for the blend films, where the lifetimes of photoexcited electrons in the NFAs follow the same order, regardless of whether the photoexcitation occurs in the acceptor (Figure 7f) or the donor (Figure 7i). The PCEs of the assembled BHJ-OSCs are ranked as **SpiroT-DCI** > **ITIC** > **SpiroF-DCI**, reflecting consistent results in the decay kinetics of free carriers. Consequently, the superior PCE of **SpiroT-DCI** could also be attributed to the prolonged lifetime of these free carriers.

Conclusions

In summary, to investigate the effect that the electronic structures of NFAs exert on the E_b and on OSC characteristics, we designed and synthesized novel **ITIC**-based NFAs with spiro-substituted bithiophene or biphenyl units as side groups. Theoretical calculations indicated that the HOMO and LUMO of **SpiroF-DCI** and **ITIC** are distributed in the main π-conjugated framework. By contrast, when electron-donating bithiophene units were introduced into **SpiroT-DCI**, they adopted a HOMO distribution, which led to detached HOMO and LUMO distributions. Electrochemical and photophysical measurements of **SpiroT-DCI** showed an upshifted HOMO energy level and a narrower E_g^{opt}, respectively, compared with those of **SpiroF-DCI** and **ITIC**. Based on the results of EA, IP, and E_g^{opt} in films, the **SpiroT-DCI** showed a E_b of 0.32 eV, which is smaller than that of either **SpiroF-DCI** (0.40 eV) or **ITIC** (0.41 eV). MD simulations indicated that **SpiroT-DCI** and **SpiroF-DCI** tend to adopt similar intermolecular configurations. Based on this result, we attributed the small E_b for **SpiroT-DCI** to the separated distribution of FMOs. This phenomenon shows that **SpiroT-DCI**-based SC-OSC were significantly improved compared with those of **SpiroF-DCI**- and **ITIC**-based devices. Furthermore, BHJ-OSCs based on PBDB-T and **SpiroT-DCI** achieved a maximum PCE of 9.08 %. Time-resolved IR absorption spectroscopy and PL decay of the pristine films revealed that intermolecular charge separation of **SpiroT-DCI** is more efficient than that of **SpiroF-DCI**. In the time-resolved IR absorption spectroscopy measurements of the blend films with PBDB-T, **SpiroT-DCI** showed a lifetime of free carriers that was longer than that of either **SpiroF-DCI** or **ITIC**. These results demonstrate that tuning FMOs to increase the electron–hole distance in the molecule is an effective molecular design for reducing the E_b of organic semiconductors, which could pave the way to the development of higher-performing OSCs.

Supporting Information

The data that support the findings of this study are available in the supplementary material of this article.

Acknowledgements

This work was supported by JSPS KAKENHI (20H02814, 20H05841, 20KK0123, 23 K17947, 20 K15352, 23H02064, JP20H05839, JP22H00344, JP20H05835, 24H00482, 20H05838, and 24H00485), NEDO (21500248-0), JST (JPMJMI22I1, JPMJSF23B3), JST, CREST (JPMJCR20R1, JPMJCR23I6), and the Mitsubishi Foundation (202310004). We acknowledge the support of AIRC center, SANKEN, Osaka University. Thanks are extended to the CAC, SANKEN, for assistance in obtaining high resolution mass spectra.

Conflict of Interest

The authors declare no conflict of interest.

Data Availability Statement

The data that support the findings of this study are available in the supplementary material of this article.

Keywords: organic solar cells · exciton binding energies · organic semiconductors · non-fullerene acceptors · exciton

[1] A. Polman, M. Knight, E. C. Garnett, B. Ehrler, W. C. Sinke, *Science* **2016**, *352*, aad4424.
[2] C. Yan, S. Barlow, Z. Wang, H. Yan, A. K.-Y. Jen, S. R. Marder, X. Zhan, *Nat. Rev. Mater.* **2018**, *3*, 1–19.
[3] P. Cheng, G. Li, X. W. Zhan, Y. Yang, *Nat. Photonics* **2018**, *12*, 131–142.
[4] J. Q. Zhang, H. S. Tan, X. G. Guo, A. Facchetti, H. Yan, *Nat. Energy* **2018**, *3*, 720–731.
[5] O. Inganas, *Adv. Mater.* **2018**, *30*, 1800388.
[6] G. Bianchi, C. Carbonera, L. Ciammaruchi, N. Camaioni, N. Negarville, F. Tinti, G. Forti, A. Nitti, D. Pasini, A. Facchetti, R. M. Pankow, T. J. Marks, R. Po, *Solar RRL* **2022**, *6*, 2200643.
[7] Y. Liu, P. Cheng, T. Li, R. Wang, Y. Li, S.-Y. Chang, Y. Zhu, H.-W. Cheng, K.-H. Wei, X. Zhan, B. Sun, Y. Yang, *ACS Nano* **2019**, *13*, 1071–1077.
[8] W. Song, B. Fanady, R. Peng, L. Hong, L. Wu, W. Zhang, T. Yan, T. Wu, S. Chen, Z. Ge, *Adv. Energy Mater.* **2020**, *10*, 2000136.
[9] S. Jinnai, A. Oi, T. Seo, T. Moriyama, M. Terashima, M. Suzuki, K. Nakayama, Y. Watanabe, Y. Ie, *ACS Sustain. Chem. Eng.* **2023**, *11*, 1548–1556.
[10] S. Jinnai, N. Shimohara, K. Ishikawa, K. Hama, Y. Iimuro, T. Washio, Y. Watanabe, Y. Ie, *Faraday Discuss.* **2024**, *250*, 220–232.
[11] G. Yu, J. Gao, J. C. Hummelen, F. Wudl, A. J. Heeger, *Science* **1995**, *270*, 1789–1791.
[12] J. J. M. Halls, K. Pichler, R. H. Friend, S. C. Moratti, A. B. Holmes, *Appl. Phys. Lett.* **1996**, *68*, 3120–3122.
[13] G. Zhang, J. Zhao, P. C. Y. Chow, K. Jiang, J. Zhang, Z. Zhu, J. Zhang, F. Huang, H. Yan, *Chem. Rev.* **2018**, *118*, 3447–3507.
[14] Y. Cui, Y. Xu, H. Yao, P. Bi, L. Hong, J. Zhang, Y. Zu, T. Zhang, J. Qin, J. Ren, Z. Chen, C. He, X. Hao, Z. Wei, J. Hou, *Adv. Mater.* **2021**, *33*, 2102420.
[15] L. Zhu, M. Zhang, J. Xu, C. Li, J. Yan, G. Zhou, W. Zhong, T. Hao, J. Song, X. Xue, Z. Zhou, R. Zeng, H. Zhu, C.-C. Chen, R. C. I. MacKenzie, Y. Zou, J. Nelson, Y. Zhang, Y. Sun, F. Liu, *Nat. Mater.* **2022**, *21*, 656–663.
[16] J. Wang, X. Zhan, *Acc. Chem. Res.* **2021**, *54*, 132–143.
[17] H. T. Wang, J. R. Cao, J. S. Yu, Z. H. Zhang, R. Y. Geng, L. Q. Yang, W. H. Tang, *J. Mater. Chem. A* **2019**, *7*, 4313–4333.
[18] P. Murugan, T. Hu, X. Hu, Y. Chen, *J. Mater. Chem. A* **2022**, *10*, 17968–17987.
[19] G. Forti, A. Nitti, P. Osw, G. Bianchi, R. Po, D. Pasini, *Int. J. Mol. Sci.* **2020**, *21*, 8085.
[20] C. J. Brabec, S. Gowrisanker, J. J. Halls, D. Laird, S. Jia, S. P. Williams, *Adv. Mater.* **2010**, *22*, 3839–3856.
[21] S. R. Forrest, *Phil. Trans. R. Soc. A* **2015**, *373*, 20140320.
[22] R. Meng, Y. Li, C. Li, K. Gao, S. Yin, L. Wang, *Phys. Chem. Chem. Phys.* **2017**, *19*, 24971–24978.
[23] S. E. Gledhill, B. Scott, B. A. Gregg, *J. Mater. Res.* **2005**, *20*, 3167–3179.
[24] P. K. Nayak, *Synth. Met.* **2013**, *174*, 42–45.
[25] S. M. Menke, N. A. Ran, G. C. Bazan, R. H. Friend, *Joule* **2018**, *2*, 25–35.
[26] T. Y. Huang, Y. M. Bai, J. Wang, F. Z. Wang, M. L. Dai, F. Han, S. X. Du, *Sol. Energy* **2021**, *230*, 628–634.
[27] B. Carsten, J. M. Szarko, H. J. Son, W. Wang, L. Lu, F. He, B. S. Rolczynski, S. J. Lou, L. X. Chen, L. Yu, *J. Am. Chem. Soc.* **2011**, *133*, 20468–20475.
[28] M. Knupfer, *Appl. Phys. A* **2003**, *77*, 623–626.
[29] Y. Zhu, F. Zhao, W. Wang, Y. Li, S. Zhang, Y. Lin, *Adv. Energy Sustainability Res.* **2022**, *3*, 2100184.
[30] P. J. Leenaers, A. Maufort, M. M. Wienk, R. A. J. Janssen, *J. Phys. Chem. C* **2020**, *124*, 27403–27412.
[31] J. Zhang, J. Guan, Y. Zhang, S. Qin, Q. Zhu, X. Kong, Q. Ma, X. Li, L. Meng, Y. Yi, J. Zheng, Y. Li, *J. Phys. Chem. Lett.* **2022**, *13*, 8816–8824.
[32] T. Li, K. Wang, G. Cai, Y. Li, H. Liu, Y. Jia, Z. Zhang, X. Lu, Y. Yang, Y. Lin, *JACS Au* **2021**, *1*, 1733–1742.
[33] S. Jinnai, K. Murayama, K. Nagai, M. Mineshita, K. Kato, A. Muraoka, A. Yamakata, A. Saeki, Y. Kobori, Y. Ie, *J. Mater. Chem. A* **2022**, *10*, 20035–20047.
[34] Y. Lin, J. Wang, Z.-G. Zhang, H. Bai, Y. Li, D. Zhu, X. Zhan, *Adv. Mater.* **2015**, *27*, 1170–1174.
[35] J.-L. Wang, H.-J. Zhang, S. Liu, K.-K. Liu, F. Liu, H.-B. Wu, Y. Cao, *Solar RRL* **2018**, *2*, 1800108.
[36] J.-D. Chai, M. Head-Gordon, *Phys. Chem. Chem. Phys.* **2008**, *10*, 6615–6620.
[37] Y. Shi, Y. Chang, K. Lu, Z. Chen, J. Zhang, Y. Yan, D. Qiu, Y. Liu, M. A. Adil, W. Ma, X. Hao, L. Zhu, Z. Wei, *Nat. Commun.* **2022**, *13*, 3256.
[38] T. Le Bahers, C. Adamo, I. Ciofini, *J. Chem. Theory Comput.* **2011**, *7*, 2498–2506.
[39] X. Tang, L.-S. Cui, H.-H. Li, A. J. Gillett, F. Auras, Y.-K. Qu, C. Zhong, S. T. E. Jones, Z.-Q. Jiang, R. H. Friend, L.-S. Liao, *Nat. Mater.* **2020**, *19*, 1332–1338.
[40] S. Kraner, G. Prampolini, G. Cuniberti, *J. Phys. Chem. C* **2017**, *121*, 17088–17095.
[41] A. J. Bard, L. R. Faulkner, *ELECTROCHEMICAL METHODS: Fundamentals and Applications*, Wiley, New York, **1984**
[42] H. Yoshida, *Chem. Phys. Lett.* **2012**, *539*, 180–185.
[43] H. Yoshida, *Anal. Bioanal. Chem.* **2014**, *406*, 2231–2237.
[44] H. Yoshida, *J. Electron Spectrosc. Relat. Phenom.* **2015**, *204*, 116–124.
[45] J.-P. Yang, F. Bussolotti, S. Kera, N. Ueno, *J. Phys. D* **2017**, *50*, 423002.
[46] Y. Tamai, R. Shirouchi, T. Saito, K. Kohzuki, S. Natsuda, *J. Mater. Chem. A* **2023**, *11*, 17581–17593.
[47] M. C. Scharber, D. Mühlbacher, M. Koppe, P. Denk, C. Waldauf, A. J. Heeger, C. J. Brabec, *Adv. Mater.* **2006**, *18*, 789–794.
[48] X. Peng, F. Song, E. Lu, Y. Wang, W. Zhou, J. Fan, Y. Gao, *J. Am. Chem. Soc.* **2005**, *127*, 4170–4171.
[49] A. C. Benniston, A. Harriman, D. J. Lawrie, A. Mayeux, *Phys. Chem. Chem. Phys.* **2004**, *6*, 51–57.
[50] Y.-Y. Wu, Y. Chen, G.-Z. Gou, W.-H. Mu, X.-J. Lv, M.-L. Du, W.-F. Fu, *Org. Lett.* **2012**, *14*, 5226–5229.
[51] A. Sugie, K. Nakano, K. Tajima, I. Osaka, H. Yoshida, *J. Phys. Chem. Lett.* **2023**, *14*, 11412–11420.
[52] D. P. Qian, L. Ye, M. J. Zhang, Y. R. Liang, L. J. Li, Y. Huang, X. Guo, S. Q. Zhang, Z. A. Tan, J. H. Hou, *Macromolecules* **2012**, *45*, 9611–9617.
[53] W. Zhao, S. Li, H. Yao, S. Zhang, Y. Zhang, B. Yang, J. Hou, *J. Am. Chem. Soc.* **2017**, *139*, 7148–7151.
[54] G. G. Malliaras, J. R. Salem, P. J. Brock, C. Scott, *Phys. Rev. B* **1998**, *58*, 13411–13414.
[55] C. Goh, R. J. Kline, M. D. McGehee, E. N. Kadnikova, J. M. J. Fréchet, *Appl. Phys. Lett.* **2005**, *86*, 122110.
[56] S. D. Dimitrov, J. R. Durrant, *Chem. Mater.* **2014**, *26*, 616–630.
[57] J.-L. Wu, F.-C. Chen, Y.-S. Hsiao, F.-C. Chien, P. Chen, C.-H. Kuo, M. H. Huang, C.-S. Hsu, *ACS Nano* **2011**, *5*, 959–967.
[58] C. M. Proctor, C. Kim, D. Neher, T.-Q. Nguyen, *Adv. Funct. Mater.* **2013**, *23*, 3584–3594.

[59] G. Kupgan, X. K. Chen, J. L. Brédas, *Mater. Today* **2021**, *11*, 100154.
[60] G. Han, Y. Guo, X. Song, Y. Wang, Y. Yi, *J. Mater. Chem. C* **2017**, *5*, 4852–4857.
[61] T. Mani, D. C. Grills, M. D. Newton, J. R. Miller, *J. Am. Chem. Soc.* **2015**, *137*, 10979–10991.
[62] Y. Song, X. Liu, Y. Li, H. H. Nguyen, R. Duan, K. J. Kubarych, S. R. Forrest, J. P. Ogilvie, *J. Phys. Chem. Lett.* **2021**, *12*, 3410–3416.
[63] C. C. S. Chan, C. Ma, X. Zou, Z. Xing, G. Zhang, H.-L. Yip, R. A. Taylor, Y. He, K. S. Wong, P. C. Y. Chow, *Adv. Funct. Mater.* **2021**, *31*, 2107157.
[64] J. Clark, C. Silva, R. H. Friend, F. C. Spano, *Phys. Rev. Lett.* **2007**, *98*, 206406.
[65] S. Cook, A. Furube, R. Katoh, *Energy Environ. Sci.* **2008**, *1*, 294–299.
[66] A. Yamakata, K. Kato, T. Urakami, S. Tsujimura, K. Murayama, M. Higashi, H. Sato, Y. Kobori, Y. Umeyama, H. Imahori, *Chem. Sci.* **2024**, *15*, 12686–12694.

Manuscript received: July 5, 2024
Accepted manuscript online: August 12, 2024
Version of record online: ■■, ■■

Research Article

Solar Cells

K. Wang, S. Jinnai,* T. Urakami, H. Sato, M. Higashi, S. Tsujimura, Y. Kobori, R. Adachi, A. Yamakata, Y. Ie* e202412691

Nonfullerene Acceptors Bearing Spiro-Substituted Bithiophene Units in Organic Solar Cells: Tuning the Frontier Molecular Orbital Distribution to Reduce Exciton Binding Energy

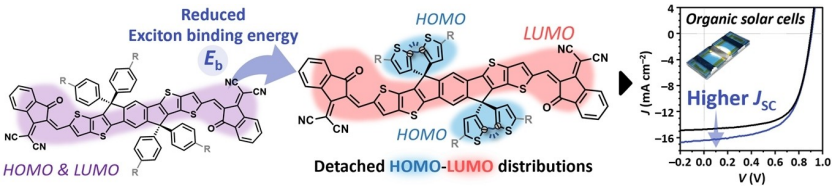

Exciton binding energy (E_b) is a key parameter for efficient charge-carrier generation in organic solar cells (OSCs). To tune the electronic structures for reducing E_b, we developed new nonfullerene acceptor (NFA) featuring spiro-substituted bithiophenes. This NFA showed the separated frontier molecular orbitals, effectively lowering the E_b. Single-component and bulk-heterojunction OSCs based on this NFA showed enhanced photovoltaic performance.